Source of Acquisition
NASA Goddard Space Flight Center

Aerosol radiative effects on deep convective clouds and associated radiative forcing

Fan, J., R. Zhang, W.-K. Tao, K. I. Mohr

Submitted to J. Geophy. Res

Popular Summary

Aerosols and especially their effect on clouds are one of the key components of the climate system and the hydrological cycle [*Ramanathan et al.,* 2001]. Yet, the aerosol effect on clouds remains largely unknown and the processes involved not well understood. A recent report published by the National Academy of Science states "*The greatest uncertainty about the aerosol climate forcing - indeed, the largest of all the uncertainties about global climate forcing - is probably the indirect effect of aerosols on clouds NRC [2001].*" The aerosol effect on clouds is often categorized into the traditional "first indirect (i.e., Twomey)" effect on the cloud droplet sizes for a constant liquid water path and the "semi-direct" effect on cloud coverage. The aerosol effect on precipitation processes, also known as the second type of aerosol indirect effect, is even more complex, especially for mixed-phase convective clouds. In this paper, the aerosol radiative effects (ARE) on the deep convective clouds are investigated by using a spectral-bin cloud-resolving model (CRM) coupled with a radiation scheme and an explicit land surface model.

The sensitivity of cloud properties and the associated radiative forcing to aerosol single-scattering albedo (SSA) are examined. The ARE on cloud properties is pronounced for mid-visible SSA of 0.85. Relative to the case excluding the ARE, cloud fraction and optical depth decrease by about 18% and 20%, respectively. Cloud droplet and ice particle number concentrations, liquid water path (LWP), ice water path (IWP), and droplet size decrease significantly when the ARE is introduced. The ARE causes a surface cooling of about 0.35 K and significantly high heating rates in the lower troposphere (about 0.6 K day-1 higher at 2 km), both of which lead to a more stable atmosphere and hence weaker convection. The weaker convection and the more desiccation of cloud layers explain the less cloudiness, lower cloud optical depth, LWP and IWP, smaller droplet size, and less precipitation. The daytime-mean direct forcing induced by black carbon is about 2.2 W m-2 at the top of atmosphere (TOA) and -17.4 W m-2 at the surface for SSA of 0.85. The semi-direct forcing is positive, about 10 and 11.2 W m-2 at the TOA and surface, respectively. Both the TOA and surface total radiative forcing values are strongly negative for the deep convective clouds, attributed mostly to aerosol indirect forcing. Aerosol direct and semi-direct effects are very sensitive to SSA. Because the positive semi-direct forcing compensates the negative direct forcing at the surface, the surface temperature and heat fluxes decrease less significantly with the increase of aerosol absorption (decreasing SSA). The cloud fraction, optical depth, convective strength, and precipitation decrease with the increase of absorption, resulting from a more stable and dryer atmosphere due to enhanced surface cooling and atmospheric heating.

Aerosol Optical Effects on Deep Convective Clouds and Radiative Forcing

Jiwen Fan[1], Renyi Zhang[1], Wei-Kuo Tao[2], and Karen I. Mohr[3]

[1] Department of Atmospheric Sciences, Texas A&M University, College Station, TX 77843

[2] NASA Goddard Space Flight Center, Code 613.1, Greenbelt, Maryland USA 20771

[3] Department of Earth and Atmospheric Sciences, University at Albany, SUNY, Albany, NY 12222

Abstract. The aerosol radiative effects (ARE) on the deep convective clouds are investigated by using a spectral-bin cloud-resolving model (CRM) coupled with a radiation scheme and an explicit land surface model. The sensitivity of cloud properties and the associated radiative forcing to aerosol single-scattering albedo (SSA) are examined. The ARE on cloud properties is pronounced for mid-visible SSA of 0.85. Relative to the case excluding the ARE, cloud fraction and optical depth decrease by about 18% and 20%, respectively. Cloud droplet and ice particle number concentrations, liquid water path (LWP), ice water path (IWP), and droplet size decrease significantly when the ARE is introduced. The ARE causes a surface cooling of about 0.35 K and significantly high heating rates in the lower troposphere (about 0.6 K day^{-1} higher at 2 km), both of which lead to a more stable atmosphere and hence weaker convection. The weaker convection and the more desiccation of cloud layers explain the less cloudiness, lower cloud optical depth, LWP and IWP, smaller droplet size, and less precipitation. The daytime-mean direct forcing induced by black carbon is about 2.2 W m^{-2} at the top of atmosphere (TOA) and -17.4 W m^{-2} at the surface for SSA of 0.85. The semi-direct forcing is positive, about 10 and 11.2 W m^{-2} at the TOA and surface, respectively. Both the TOA and surface total radiative forcing values are strongly negative for the deep convective clouds, attributed mostly to aerosol indirect forcing. Aerosol direct and semi-direct effects are very sensitive to SSA. Because the positive semi-direct forcing compensates the negative direct forcing at the surface, the surface temperature and heat fluxes decrease less significantly with the increase of aerosol absorption (decreasing SSA). The cloud fraction, optical depth, convective strength, and precipitation decrease with the increase of absorption, resulting from a more stable and dryer atmosphere due to enhanced surface cooling and atmospheric heating.

Keywords: Aerosol radiative effects, Aerosol radiative forcing, Aerosol-cloud interaction, Deep convective clouds

1. Introduction

Aerosols interact directly and indirectly with the Earth's radiation budget and climate. As a direct effect, aerosols scatter and absorb solar radiation [*Charlson and Pilat*, 1969; *Coakley et al.*, 1983]. As an indirect effect, aerosols act as cloud condensation nuclei (CCN) and affect cloud properties [*Twomey*, 1977; *Rosenfeld*, 2000]. Also, aerosol absorption modifies the atmospheric temperature structure, decreases the solar radiation at the surface, and lower surface moisture fluxes, which may suppress convection and reduce cloud fraction [*Ackerman et al.*, 2000; *Ramanathan et al.*, 2001b]. This phenomenon has been termed the "semi-direct effect" [*Hansen et al.*, 1997; *Johnson et al.*, 2004]. The addition of anthropogenic aerosols to the atmosphere may change the radiative fluxes at the top-of-atmosphere (TOA), at the surface, and within the atmospheric column. Recent reports summarize that on a global average the sum of direct and indirect forcing by anthropogenic aerosols (ACF) at the TOA is likely to be negative and may be comparable in magnitude to the positive forcing of about 2.4 W m^{-2} by anthropogenic greenhouse gases [*IPCC*, 2001]. Large uncertainties exist in current estimates of aerosol forcing because of incomplete knowledge concerning the distribution and the physical and chemical properties of aerosols as well as aerosol-cloud interactions.

The estimation of the direct radiative forcing exerted by aerosol is complex to quantify because anthropogenic particles are generally a complex mixture of different chemical components [*Hegg et al.*, 1997; *Ramanathan et al.*, 2001a]. Each component is characterized by its own microphysical, chemical, and related optical properties, which lead to variable direct radiative forcing. The uncertainty for the aerosol direct climate forcing is about a factor of 2 to

3 whereas that for the indirect forcing is much larger and difficult to quantify [*IPCC*, 2001]. The global mean TOA aerosol direct forcing values range from -0.5 to +0.2 W m^{-2} [*Ramanathan et al.*, 2001b], and the measured TOA direct forcing on the regional scale ranges from -9 to 2 W m^{-2} [*Ramanathan et al.*, 2001b; *Ramachandran*, 2005]. The semi-direct effect introduces the added feedbacks due to the radiative properties of the aerosol (i.e., absorption) and has been studied in the recent years. *Ackerman et al.* [2000] showed decreases in cloudiness commensurate with the heating rates associated with the absorbing aerosol. *Johnson et al.* [2004] and *Feingold et al.* [2005] suggested that the vertical location of the absorbing aerosol is important: absorbing aerosol may reduce cloud water and cloud fraction or increase them. On the other hand, the reduction in downwelling solar radiation and associated decrease in surface latent and sensible heat fluxes result in significant reduction in cloud water and cloud fraction [*Feingold et al.* 2005; *Jiang and Feingold*, 2006]. The semi-direct forcing was estimated to be about 15 W m^{-2} for stratocumulus by *Johnson et al.* [2004] and 7.5 W m^{-2} for trade cumulus by *Ackerman et al.* [2000].

Black carbon (BC) is an important absorbing aerosol produced primarily from fossil fuel and biomass burning. In the atmosphere, BC particles interact with other aerosol particles and gas phase species and exist at various mixing states [*Zhang and Zhang*, 2005]. The impact of BC on clouds and radiative forcing depends on the mixing state. Coating on BC aerosols may significantly increase the absorption of solar radiation [*Chylek et al.*, 1995]. Three mixing treatments for BC have been discussed in literatures: externally mixed, well-internally mixed, and core-coated [*Jacobson*, 2000]. Of the three mixing types, the core-coated treatment covers

the largest range of particle configurations. *Posfai et al.* [1999] found that internally mixed soot and sulfate appear to comprise a globally significant fraction of aerosols in the troposphere. BC was commonly treated as a core coated by the other components to study aerosol radiative properties [*Ackerman and Toon*, 1981; *Jacobson*, 1999].

It has been demonstrated that the climate effects of BC aerosols are more significant on the regional scale than on the global scale [*Wang*, 2004]. A polluted urban atmosphere typically has an elevated aerosol loading because of emissions from transportation and industry [*Zhang et al.*, 2004a], which may exert significant aerosol radiative forcing. Houston, TX is one of the most polluted urban cities in the US. Houston hosts one of the world largest petrochemical complexes and several large fossil-fueled electric power plants. Transportation and industry emit a great quantity of VOCs, NO_x, and SO_2 [*Li et al.*, 2005; 2007; *Zhang et al.*, 2004b]. In association with the Texas 2000 Air Quality Study (TexAQS 2000), there exist several ground-based and aircraft measurements of aerosol compositions, number size distributions, and optical properties [*Brock et al.*, 2003; *Fast et al.*, 2006]. High aerosol number concentrations (over 10^5 cm^{-3}) have been identified to exist in this area, associated with transportation and industrial activities [*Brock et al.*, 2003; *Fan et al.*, 2006]. The observed BC mass concentrations at LaPorte in Houston were high up to 2.0 $\mu g\ m^{-3}$ [*Fast et al.*, 2006], and the simulated mass mixing ratio of BC to ammonium sulfate was high up to 1:8 [*Fan et al.*, 2005]. The effect of anthropogenic aerosols on direct radiative forcing is significant in the vicinity and downwind of the urban area of Houston. The observed aerosol radiation forcing during the afternoon periods was between -30 and -80 $W\ m^{-2}$ [*Fast et al.*, 2006]. *Fast et al.*

[2006] also indicated that the predicted shortwave radiation was 30 to 40 W m^{-2} closer to the observations in the vicinity of Houston when the aerosol radiative properties were incorporated into the shortwave radiation scheme.

We have previously investigated the aerosol indirect effect on the cumulus clouds in the Houston area using a two-dimensional cloud-resolving Goddard Cloud Ensemble (GCE) model with the spectral-bin cloud microphysics [*Fan et al.*, 2007a; b]. In this paper, a more comprehensive investigation of aerosol effects on deep convective clouds is performed by incorporating the radiative transfer processes and the land-atmosphere interaction processes into the above-mentioned GCE model, with the focus on radiative effects of anthropogenic aerosol containing BC. An aerosol radiative module is developed to calculate the wavelength-dependent aerosol radiative properties based on the aerosol composition, size distribution, mixing state, and ambient relative humidity. The significance of the aerosol radiative effects (ARE) is investigated by comparing with the case excluding the ARE. The associated aerosol direct, semi-direct and indirect radiative forcing values for deep convective clouds are estimated, and the sensitivity of cloud properties and radiative forcing to aerosol single-scattering albedo (SSA) are examined. Although the effects of aerosols including absorbing components on clouds and radiative forcing have been investigated by model simulations in previous studies [*Johnson et al.*, 2004; *Feingold et al.* 2005; *Jiang and Feingold*, 2006; *McFarquhar and Wang*, 2006], few studies have simultaneously examined the aerosol direct, semi-direct, and indirect effects on clouds using a spectral-bin CRM coupled with a state-of-the-art land surface model and an aerosol radiative module to online calculate the

aerosol radiative properties.

2. Model Description

The GCE model employed in the present study is 2-D and nonhydrostatic. The description of the model dynamics and microphysics has been presented in *Fan et al.* [2007a], and more details on those processes can also be found in *Khain et al.* [2004] and *Tao et al.* [2003a]. The spectral-bin microphysics is based on solving an equation system for eight number size distributions for water drops, ice crystals (columnar, plate-like and dendrites), snowflakes, graupel, hail/frozen drops and aerosols/CCN. Each size distribution is represented by 33 mass doubling bins. Originally, the initial aerosol size distribution is calculated by an empirical formula: $N = N_0 S_w^k$ [*Pruppacher and Klett*, 1997], where S_w is the supersaturation with respect to water, and the CCN activation is calculated for single-component aerosols according to the Köhler theory. We have modified the initial aerosol size distribution and CCN activation, as discussed in our previous studies [*Fan et al.*, 2007a, b], to reflect the aerosol/CCN characteristics in this region. The activation schemes for multiple-component soluble aerosols and aerosols with a slightly soluble or insoluble core have been incorporated into the GCE model to investigate the effects of aerosol compositions on clouds [*Fan et al.*, 2007a].

The GCE model employed in this study has been further updated by incorporating a Goddard radiation scheme and an explicit Goddard land surface model of a Parameterization for Land-Atmosphere-Cloud Exchange (PLACE) [*Wetzel and Boone*, 1995; *Tao et al.*, 2003a], to investigate the aerosol radiative effects on deep convective clouds and the associated forcing.

An aerosol radiative module has been developed and coupled into the radiation scheme to on-line calculate the wavelength-dependent aerosol optical depth (AOD), single-scattering albedo (SSA), and asymmetry factor (AF) based on the aerosol characteristics and ambient relative humidity.

2.1 PLACE land surface model and Goddard radiation scheme

The PLACE model is a detailed interactive process model of the heterogeneous land surface (soil and vegetation) and adjacent near-surface atmosphere. PLACE consists of linked process models (e.g., net radiation, evapotranspiration, ground heat storage) and emphasizes the vertical transport of moisture and energy through the 5 layer soil moisture and the 7 layer soil temperature column to the overlying heterogeneous land surface. The additional two soil temperature layers are used to aid in resolving large temperature gradients near the surface. Momentum, sensible, and latent heat fluxes are calculated using similarity relationships [*Zilitinkevich*, 1975; *Businger et al.*, 1991]. More details on the description of PLACE can be found in *Wetzel and Boone* [1995]. The atmospheric component of GCE provides surface winds, surface air temperature, surface pressure, moisture, shortwave and longwave radiation, and precipitation to the land surface model (PLACE). The land surface component returns momentum, sensible heat, and latent heat fluxes to the atmosphere. The coupling is two-way interactive. A 2-D GCE coupled with the PLACE model has previously been used to investigate landscape-generated deep convection [*Lynn et al.*, 1998; *Baker et al.*, 2001] and the sensitivity of convection to land cover in the semi-arid regions of West Africa [*Mohr et al.*, 2003; *Alonge et al.*, 2007].

The latest version of the Goddard radiation scheme includes shortwave and longwave

radiation models [*Tao et al.*, 2003a, b]. The shortwave radiation model of *Chou and Suarez* [1999] is used to compute the solar fluxes due to absorption and scattering by clouds, aerosols and gases (including water vapor). Fluxes are integrated virtually over the entire spectrum, from 0.175 to 10 μm. The spectrum is divided into seven bands in the ultraviolet (UV) region (0.175–0.4 μm), one band in the photosynthetically active radiation (PAR) region (0.4–0.7 μm), and three bands in the near infrared region (0.7–10.0 μm). In the UV and PAR region, a single O_3 absorption coefficient and a Rayleigh scattering coefficient are used for each of the eight bands. In the infrared wavelength range, the *k*-distribution method is applied to compute the absorption of solar radiation. Reflection and transmission of a cloud and aerosol-laden layer are computed using the δ-Eddington approximation. Fluxes for a composite of layers are then computed using the two-stream adding approximation. The longwave radiation parameterizations developed by *Chou et al.* [1999] and *Kratz et al.* [1998] are implemented into the GCE model. The IR spectrum is divided into nine bands. In addition, a narrow band in the 17 μm region is added to compute flux reduction due to N_2O. As in the solar spectral region, the *k*-distribution method with temperature and pressure scaling is used to compute the transmission function in the weak absorption bands of water vapor and minor trace gases (N_2O, CH_4, CFC's). A look-up table method is used to compute the transmission function in the strong absorption bands.

2.2 Aerosol radiative module

The wavelength-dependent aerosol radiative properties such as AOD (τ), SSA (σ), and AF (*g*) are the key factors to determine the aerosol radiative effects on clouds and associated

forcing. Instead of using the fixed aerosol radiative properties during the simulations as in some previous studies [e.g., *Johnson et al.*, 2004; *McFarquhar and Wang*, 2006], an aerosol radiative module has been developed and incorporated into the radiation scheme to online calculate the aerosol radiative properties as a function of wavelength (λ) based on the aerosol composition, size distribution, mixing state, and ambient relative humidity. The module includes the methodologies for the external and core-coated internal mixing states. The calculations of aerosol radiative properties for the core-coated internal mixture are presented below.

For the internally mixed aerosol components, the complex refractive index of aerosol particles is calculated based on the volume-weighted average of the individual refractive index [*Hänel*, 1976]. The real and imaginary parts of the complex refractive index, denoted by $\bar{n}(i,\lambda)$ and $\bar{k}(i,\lambda)$, respectively, for aerosols in a size bin (i) at a certain wavelength (λ) are determined by:

$$\bar{n}(i,\lambda)=\sum_{l=1}^{m} n(l,i,\lambda)f(l),\ \bar{k}(i,\lambda)=\sum_{l=1}^{m} k(l,i,\lambda)f(l) \qquad (1)$$

where m is the number of aerosol components and $f(l)$ is the volume fraction of the component (l). The Mie theory [*Bohren and Huffman*, 1983] is employed to calculate the extinction efficiency (Q_e), scattering efficiency (Q_s), and asymmetry factor (g) as functions of the size parameter, $x=2\pi r/\lambda$, where r is the particle's wet radius. The hygroscopic growth of a water-soluble component at a certain ambient humidity is calculated by the relation defined by *Mallet et al.* [2004],

$$r_{g,a(o)}=r_{g,a(b)}(1-h)^{e} \qquad (2)$$

where h is the relative humidity. The coefficient e depends on the considered type of aerosol. It is equal to 0.25 for particulate organic matter [*Chazette and Liousse*, 2001], and 0.285 for ammonium sulfate, nitrate, and sea salt [*Hänel*, 1976]. To avoid repeated Mie calculations, the first step of this methodology is to obtain a look-up table containing aerosol optical properties, i.e., Q_e, σ, and g, over all size ranges covered by 33 bins and a set of refractive indices that represent a range of indices typical of atmospheric aerosols by performing full Mie calculations. In all subsequent calls to this algorithm, the Mie calculations are skipped, and the Q_e, σ, and g for an aerosol particle are obtained by interpolating linearly from the look-up table with the calculated complex refractive index and size parameter.

The aerosol optical depth ($\tau(\lambda, j)$) at a certain λ and atmospheric layer (j) is calculated by integration over the aerosol particles in all of 33 size bins and given by

$$\tau(\lambda, j) = \sum_{i=1}^{33} Q_e(\lambda, r_i)\pi r_i^2 n(r_i, j)dz_j \qquad (3)$$

where $n(r_i, j)$ represents the aerosol number concentrations and dz_j is the height of the atmospheric layer. It is noted that r_i is the wet particle radius, corrected with the hygroscopic growth and calculated with eq. (2). Assuming $\tau(\lambda, r_i, j) = Q_e(\lambda, r_i)\pi r_i^2 n(r_i, j)dz_j$, the weighted-mean values of SSA (σ) and AF (g) for the aerosol mixture at a certain wavelength and layer are then calculated by

$$\sigma(\lambda, j) = \sum_{i=1}^{33} \tau(\lambda, r_i, j)\sigma(\lambda, r_i, j) \Big/ \sum_{i=1}^{33} \tau(\lambda, r_i, j) \qquad (4)$$

$$g(\lambda, j) = \sum_{i=1}^{33} \tau(\lambda, r_i, j)\sigma(\lambda, r_i, j)g(\lambda, r_i, j) \Big/ \sum_{i=1}^{33} \tau(\lambda, r_i, j)\sigma(\lambda, r_i, j) \qquad (5)$$

For the externally mixed aerosol components, the aerosol radiative properties τ, σ, and g are calculated for each component first, and the ensemble aerosol radiative properties for the total aerosol population are summed over all of the components [*Wolf*, 2002].

Once the wavelength-dependent aerosol radiative parameters τ, σ, and g are found, they are transferred to the shortwave and longwave radiative transfer models, and then interact with the other components of GCE such as dynamical, microphysical, and surface processes along with the cloud radiative properties.

3. Model Configuration and Validation

3.1 Initial conditions and design of numerical experiments

The initial sounding used in the simulations is from Lake Charles (93.21W, 30.11N) near the Houston area, and is at 7:00 am (local time) on August 24, 2000 (Figure 1). The vertical temperature and dew point profiles reveal an unstable atmosphere with convective available potential energy (CAPE) of 1800 J kg^{-1}, integrated from the level of 500 m. For an early morning sounding, the surface temperature is low (23.2°C) and the surface relative humidity is high (87%) (Figures 1a and 1b). The sounding also reveals weak wind shear (Figure 1c). The computational domain is comprised of 1024 × 33 grid points with a horizontal resolution of 500 m. There are 33 stretched vertical levels with a resolution of 280 m at the lowest level and 1260 m at the top. Open boundary conditions are used at the lateral boundaries. The

dynamic time step is 6 s. The radiation and land surface processes are calculated every 3 min.

The initial surface conditions for PLACE are broadly representative of land cover in the Houston area as shown in Table 1. In this heavily urbanized region is a mixture of impervious cover, lawns, and deciduous broadleaf trees and bushes. The soils are typical of coastal plains, sandy and silty clays and clay loams. The low percentage of vegetation cover reflects the sprawling urban infrastructure of buildings and transportation networks. Initial soil moisture and soil temperature values are based on examination of the NCEP/NCAR daily reanalysis of soil moisture, soil temperature, and precipitation for the week preceding 24 August, 2000. The reanalysis of volumetric soil moisture in the layers 0–10 cm and 10–200 cm for the Houston area has a range of 0.20–0.28 cm^3 cm^{-3}. The initial soil moisture values in Table 1 assume additional drying in the layers above 10 cm after rainfall on 22 August. Both soil temperature and moisture are randomly varied within the ranges in Table 1 across the model domain to account for the variability of the urban landscape.

A series of simulations have been performed. We first perform the control run (AR_85) considering aerosol radiative effects. The initial aerosol size distribution in AR_85 is from the modeled results and has been compared and validated with the observations [*Fan et al.*, 2006, 2007a]. Aerosols are represented by internal BC-cores surrounded by ammonium sulfate. The preliminary analysis of the recent in-situ measurements of the mixing states of BC during TexAQS 2006 shows about 70% internally mixed BC in the Houston area [*J. P. Schwarz* of NOAA, personal communication]. The mass mixing ratios are assumed to be about 0.1 for BC and 0.9 for ammonium sulfate (Table 2). The activation scheme accounting for the effect of the

insoluble core is employed to calculate CCN activation [*Fan et al.*, 2007a]. As shown in Table 2, the mid-visible (at 0.55 μm) AOD, SSA and AF calculated from the aerosol radiative module at the initial time of the simulation are 0.27, 0.85, and 0.76, respectively, consistent with the observations in Houston. Generally, the observed mid-visible AOD is between 0.25 and 0.4, and the SSA falls in the range of 0.85-0.95. In order to isolate the aerosol radiative effects, an additional simulation (NAR_00) is set to be similar with AR_85, except that the aerosol radiative properties, i.e., AOD, SSA, and AF, are set to zeroes (without calling the aerosol radiative module) (Table 2). To estimate the aerosol radiative forcing, two other simulations are performed for background aerosols (ammonium sulfate only) considering the aerosol radiative effects: one corresponds to the polluted case (SA_100) and the other corresponds to the clean case (SAC_100). SA_100 has the same initial aerosol size distribution as AR_85, but a simple Köhler theory is employed for the activation of ammonium sulfate. SAC_100 has the similar configuration with SA_100, except that the aerosol concentration is only about 7% of SA_100, which is about 3000 cm^{-3} (sum over the size distribution $dN/d\ln(D_p)$). As shown in Table 2, the AOD at 0.55 nm is 0.25 for SA_100 but is only 0.009 for SAC_100. The values of SSA are 1.0 for both cases because ammonium sulfate only has a scattering effect. An exponential decrease of aerosol concentrations with height is used as the initial condition for all of the simulations, similarly to our previous studies [*Fan et al.*, 2007a, b].

Further tests are performed for the sensitivity of aerosol radiative effects to SSA. The mass ratio of BC to ammonium sulfate is varied to yield the aerosol mixtures with a range of mid-visible SSA: 0.85, 0.9, 0.95, and 1.0 for pure ammonium sulfate. These reflect the typical

range of mid-visible SSA values observed in the atmosphere. The tests with the SSA of 0.85 and 1.0 correspond to the simulations AR_85 and SA_100, respectively. The other two tests with SSA = 0.90 and 0.95 have the similar configurations with AR_85, with the exception of different mixing ratio of BC to ammonium sulfate. The initial mid-visible AOD decreases gradually from 0.27 to 0.25 as SSA increases from 0.85 to 1.0.

All simulations have been run for 10-hr daytime, from 7:00 -17:00. The analyses are performed for the middle 6 hrs by excluding the model spin-up time, except for the forcing estimates, which are calculated based on the entire daytime simulations.

3.2 Validation of the coupled GCE model

Although the surface model PLACE and the Goddard radiation scheme have been validated separately in previously studies [*Mohr et al.*, 2003; *Alonge et al.*, 2007; Tao et al., 2003b], the fully coupled model system is validated here by comparing with the observations and other modeling results. Figure 2 shows the comparisons of the surface temperature and the downwelling surface infrared fluxes between the modeled values from AR_85 and the observed values from the site of La Porte in Houston [*Zamora et al.*, 2003; 2005]. The modeled surface temperature and the downwelling surface infrared fluxes are in generally agreement with the observations, although the model tends to slightly overestimate the surface temperature and underestimate the downwelling surface infrared fluxes. The sharp decrease in observed temperature at 480 min is attributed to a storm occurring at that site. The maximum difference in the downwelling surface infrared fluxes between the modeled and observed values is only about 10 W m^{-2}. Because of the poor data quality of the sensible and latent heat fluxes in

observations, comparisons of those parameters with the values from the MM5 simulations in the study of surface heat fluxes [*Zamora et al.*, 2003] are provided. The modeled maximum sensible and latent heat fluxes from AR_85 are about 314 and 318 W m^{-2}, occurring at 330 and 250 min, respectively. They are consistent with the values of 310 and 300 W m^{-2} at 360 and 300 min, respectively, from MM5 simulations. Also, the modeled maximum surface solar flux is 945 W m^{-2}, consistent with the observed value of 960 W m^{-2}. The good agreement of these parameters with the observations and simulations indicates that the surface model responds correctly to the changes in net radiation and the coupled system is able to provide robust simulations. The overestimation of surface temperature and the earlier peak for heat fluxes have also been observed in some other model studies with PLACE [*Mohr et al.*, 2003; *Alonge et al.*, 2007].

In addition, the simulated cloud optical depth (τ_c) is compared with the observed τ_c from MODIS satellite observations for deep convective clouds in the area. By averaging the τ_c values from 40 -100 (deep convective clouds), the model yields a value of about 69, close to the observed average value of 73 for the period of August 2002. The analysis of satellite observations indicates that the average τ_c for deep convective clouds from 2002 to 2006 does not change appreciably.

4. Results and Discussion

4.1 Aerosol radiative effects (ARE)

Comparisons are made between the simulations with (AR_85) and without the ARE

(NAR_00). Figure 3 shows the time series of cloud microphysical fields averaged over all cloudy grids from 120-480 min. Note that the aerosol composition and initial size distribution are the same for these two simulations. The differences in droplet number concentration between NAR_00 and AR_85 are insignificant since the droplet number is mainly determined by aerosol composition and size distribution (Figure 3a). However, the simulation with the ARE (AR_85) has much lower ice particle concentrations than that without the ARE (NAR_00) (Figure 3b). The liquid water path (LWP) and ice water path (IWP) for the two cases are presented in Figures 3c and 3d, respectively. The LWP is defined as the sum of the mass-integrated mixing ratios of cloud water and rain water that determine water clouds, while IWP is defined as the sum of the mass-integrated mixing ratios of ice crystal, snow, graupel, and hail that determine the ice clouds. With the inclusion of the ARE, both LWP and IWP decrease significantly (Figures 3c and 3d). Also as shown in Figure 3, the peak values of cloud microphysical properties are delayed when the ARE is considered. The averaged cloud microphysical properties over the cloudy grids and during the simulation time from 120 to 480 min are shown in Table 3. The average ice particle number concentration (N_i) in AR_85 is about 35% lower than that in NAR_00. The average LWP and IWP decrease by about 15% when including the ARE. The ice microphysical properties respond more significantly to the ARE than the warm-cloud microphysical properties. With the ARE, the droplet effective radius (r_e) becomes significantly smaller, as shown in Figure 4. The average r_e decreases from 5.9 μm in NAR_00 to 5.6 μm in AR_85 (Table 3). The vertical profile of r_e (Figure 4b) reveals that the differences in r_e are especially noticeable at heights above 6 km, probably because ice processes

are more sensitive to aerosol radiative effects.

The direct radiative effect of strongly absorbing aerosols reduces the incoming solar radiative fluxes at the surface. The reduction in the surface radiative fluxes leads to a decrease in surface heat fluxes and consequently suppresses convection. Figure 5 presents the temporal variation of the updraft velocity averaged over the grids with a velocity greater than 1.0 m/s in the simulation domain. Generally, the convective strength is significantly weaker in AR_85 than that in NAR_00. The averaged domain-maximum updraft velocity (v_{max}) during 120-480 min is about 5.0 m/s in NAR_00 and 4.6 m/s in AR_85. The comparisons of surface temperature and heat fluxes between AR_85 and NAR_00 are shown in Figure 6. With the ARE, the average surface temperature decreases by about 0.35 K. The surface sensible heat fluxes decrease by up to 28 W m^{-2}, but the latent heat fluxes decrease less significantly than the sensible heat fluxes. The decrease in surface heat fluxes suppresses convection and results in less cloudiness. Moreover, the semi-direct effect of BC heats air and leads to a more stable and dryer atmosphere, and consequently decreases cloud cover and LWP. The weaker convective strength leads to shallower clouds and then weaker ice processes, resulting in less ice particle concentrations and IWP. As show in Figure 7a, the cloud fractions (f_{cld}) averaged over the entire domain in AR_85 are significantly less than those in NAR_00. The f_{cld} decreases by about 18% on average (Table 3), with the maximum of over 60%, when the ARE is considered. The cloud optical depth (τ_c) also decreases significantly (Figure 7b), with an average value of over 20% (Table 3). Figure 8 illustrates the vertical profiles of the heating rates averaged over the simulation time of 120-480 min. The heating rates below 5 km in AR_85 are significantly

higher than those in NAR_00 due to aerosol absorption. The peak heating rate is at about 2 km with an average value of 2.7 K day^{-1} in AR_85, which is about 0.6 K day^{-1} higher than that in NAR_00. An extra 0.6 K day^{-1} of heating rate resulting from the ARE dries the atmosphere and burns the lower clouds, contributing to significant decreases in cloud fraction and cloud optical depth as shown in Figure 7. The decreases in LWP, cloud fraction, and cloud optical depth by including the ARE have also been found in *Jiang and Feingold* [2006] for warm convective clouds.

The aerosol radiative effects impact precipitation dramatically. The domain-averaged rain rate (r_{rain}) during 120-480 min is reduced by about 50% (Table 3). With the ARE (AR_85), the accumulated rain per grid shown in Figure 9 decreases by a factor of 2. The decrease in precipitation primarily results from the shallower clouds due to weaker convection and the desiccation of the cloud layers caused by aerosol semi-direct effect.

In order to estimate the aerosol radiative forcing, the simulations SA_100 and SAC_100 with the background aerosols (ammonium sulfate only) are conducted for the polluted and clean conditions, respectively, with the inclusion of the ARE. Without the absorbing component of aerosols, the cloud fraction and cloud optical depth shown in Figure 7 for SA_100 are close to those for NAR_00, but significantly higher than those for AR_85. The clean case (SAC_100) has the largest cloud cover and lowest cloud optical depth, relating to much more convective cells and much larger droplet sizes (Figure 7 and Table 3). The simulations without the absorbing component of aerosols (i.e., SA_100 and SAC_100) have the similar vertical profiles of the heating rates with the simulation without the ARE (NAR_00), as shown in Figure 8. The

difference in the average surface temperature between the SA_100 and NAR_00 is about 0.25 K, and the differences in the sensible and latent heat fluxes are only a few W m^{-2}. Therefore, the scattering effect of ammonium sulfate on surface heat fluxes is small. Also as shown in Table 3, SA_100 has a higher cloud droplet number concentration (253.3 cm^{-3}) than NAR_00 (191.2 cm^{-3}), resulting from the CCN activation processes. The higher droplet number concentrations are responsible for the smaller droplet size in SA_100. Although the clean case (SAC_100) has a lower cloud droplet and ice particle number concentration, LWP and IWP are higher because of the higher mass content of liquid water and ice water due to efficient growth (Table 3). However, compared with three polluted cases (NAR_00, AR_85, and SA_100), the ice particle number concentrations and IWP in SAC_100 are much lower, indicating a weaker ice process in the clean case due to much less droplet number concentrations and much stronger warm rain processes (coalescence). Figure 9 shows much more precipitation for the clean case than for the polluted cases. In contrast to the increases in convection and precipitation with aerosols in our previous study of aerosol indirect effects on a warm-bubble initiated cumulus cloud [*Fan et al.*, 2007b], the convection and precipitation are suppressed by aerosols for the clouds induced by the surface heating through radiation, consistent with the study by *Jiang and Feingold* [2006] for warm convective clouds.

Separate estimates of the direct, semi-direct, and indirect forcing values at the TOA and surface (SFC) are made based on the definitions in *McFarquhar and Wang* [2006]. The total forcing (f_{total}) is the difference in the net radiative fluxes between the simulation for the polluted air with BC (AR_85) and the simulation with the clean background aerosols (SAC_100). The

combination of the direct and semi-direct forcing, $f_{direct+semi}$, is defined as the difference in the net fluxes between the simulation for the polluted air with BC (AR_85) and the simulation with the polluted background aerosols (SA_100). The difference in the net fluxes between the simulation with the polluted background aerosols (SA_100) and the simulation with the clean background aerosols (SAC_100) corresponds to the non-absorbing aerosol indirect forcing ($f_{indirect}$). The direct forcing of BC, f_{direct}, is derived from the difference in the clear-sky net fluxes between the simulations of the polluted air with BC (AR_85) and the polluted background aerosols (SA). Table 4 summarizes the calculated forcing values for AR_85 averaged over the entire domain and during the daytime (from 7:00 to 17:00 local time). The total aerosol radiative forcing, f_{total}, at the TOA and surface are –11.6 and –31.9 W m^{-2}, respectively, in good agreement with the values of -9 W m^{-2} at the TOA and -30 W m^{-2} at the surface reported over the Bay of Bengal where the aerosols consisted of soot, sulfate, and organics [*Ramachandran*, 2005]. The semi-direct forcing of BC, f_{semi}, is 10.0 W m^{-2} at the TOA and 11.2 W m^{-2} at the surface. The direct forcing induced by BC is positive (2.2 W m^{-2}) at the TOA, but is strongly negative at the surface (-17.4 W m^{-2}). The sum of direct and semi-direct forcing, $f_{direct+semi}$, warms the TOA by 12.2 W m^{-2} and cools the surface by a smaller magnitude (-6.2 W m^{-2}). Because the semi-direct forcing compensates the direct forcing at the surface, the reduction of the surface fluxes due to the ARE is not so significant, as shown in Figure 6. Compared with the semi-direct forcing estimates of 15 W m^{-2} for stratocumulus by *Johnson et al.* [2004] and of 7.5 W m^{-2} for the trade cumulus by *Ackerman et al.* [2000] at the surface, the estimates of 11.2 W m^{-2} reported in the present work is close to the median value between the

previous studies. *Xu et al.* [2003] reported a daily-mean surface direct radiative forcing of -11.2 W m^{-2} over Yangtze delta region in China, slightly higher than our daily-mean value of -8.7 W m^{-2} estimated from the daytime-mean value of -17.4 W m^{-2} because of a larger AOD. The TOA indirect radiative forcing ($f_{indirect}$) is estimated to be -23.8 W m^{-2} and the surface $f_{indirect}$ is about -25.7 W m^{-2}, much higher than those reported over the tropical Indian Ocean (INDOEX) by *Ramanathan et al.* [2001b]. For much more polluted air in Houston, the aerosol indirect forcing should be higher than that for the INDOEX case.

4.2 Sensitivity to SSA

Table 5 shows the TOA and surface solar radiative fluxes averaged over the entire domain and during the daytime for the simulations with different SSA and the relative net fluxes to the pure ammonium sulfate case (i.e., SSA = 1.0). At the TOA, the upwelling fluxes ($F^{\uparrow}$(TOA)) are reduced with the decrease of SSA due to the increase of aerosol absorption, leading to an increase in the net solar radiative fluxes (F_{net}(TOA)). The net TOA solar radiative flux increases by 14.05 W m^{-2} when SSA decreases from 1.0 to 0.85, while the net surface solar radiative flux decreases by 5.81 W m^{-2} because of the decrease of the downwelling radiative flux ($F^{\downarrow}$(SFC)) due to the increase of absorption (Table 5). Increasing aerosol absorption leads to higher heating rates in the lower troposphere (Figure 10). The heating rate at 2 km for SSA = 0.85 is about 0.5 K day^{-1} higher than that for SSA = 1.0. At the surface, the heating rate for SSA = 0.85 is also about 0.3 K day^{-1} higher. This surface heating compensates the negative direct forcing, causing the surface temperature to be insensitive to SSA. As shown in Table 6, the average surface temperature (T_{sfc}) decreases slightly from 306.09 to 305.98 K as SSA decreases from

1.0 to 0.85. Consequently, the decreases in the surface sensible (F_{SH}) and latent heat fluxes (F_{LH}) with the decrease of SSA are insignificant (Table 6). *Huang et al.* [2007] also found that the surface temperature did not change much because of the canceling effect of semi-direct forcing, consistent with the results reported here.

Figure 11 illustrates the aerosol radiative forcing versus SSA at the TOA (Figure 11a) and surface (Figure 11b). All the forcing values correspond to the daytime-means. Aerosol absorption generates significant positive direct and semi-direct radiative forcing at the TOA, and the semi-direct effect overwhelms the direct effect for moderately or strongly absorbing aerosol mixtures (Figure 11a). The sum of the direct and semi-direct forcing yields only about 0.6 W m^{-2} positive TOA forcing at SSA = 0.95, but the value increases to 12.1 W m^{-2} at SSA = 0.85. The TOA total radiative forcing values are strongly negative for all SSA cases due to the aerosol indirect effect (Figure 11a). The indirect effect related increase in cloud albedo, and subsequently negative TOA forcing, dominates the positive TOA direct and semi-direct forcing above the clouds for this case. This is in agreement with the investigation by *Keil and Haywood* [2003] of the radiative forcing of biomass-burning aerosols in Southern African. Also seen from Figure 11a, there is significantly less negative TOA forcing with the decrease of SSA due to the absorption of aerosols induced by BC (semi-direct effect).

At the surface, BC leads to strongly negative direct forcing and the value is up to 17.4 W m^{-2} at SSA = 0.85 (Figure 11b). However, the positive semi-direct forcing partially compensates the negative direct forcing. Thus, the sum of direct and semi-direct forcing is much less negative, with a value of –6.2 W m^{-2} at SSA = 0.85. *Johnson et al.* [2004] indicated

that for marine stratocumulus the semi-direct forcing may well exceed the direct forcing even for moderately absorbing aerosols. Both direct and semi-direct effects are very sensitive to SSA at the surface. Note that aerosol indirect forcing is dominant for the deep convective clouds. Therefore, the surface total radiative forcing is much more negative by including the indirect effects, but it is not as sensitive to SSA as the TOA total forcing, due to the compensation of positive semi-direct forcing. The more strongly negative surface radiative forcing for the lower SSA cools the surface and decreases the sensible and latent heat fluxes, leading to weaker convection, less cloudiness and hence lower cloud albedo. These effects are enhanced by the semi-direct effect of absorbing aerosols, which warms air, enhances the stability of the lower atmosphere, and dries the lower cloud layer. As shown in Table 6, the averaged domain-maximum updraft velocity during 120-480 min decreases from 4.82 m/s to 4.56 m/s, and the cloud fraction decreases from 0.18 to 0.15 with the decrease of SSA from 1.0 to 0.85. The domain-averaged cloud optical depth decreases from 5.06 at SSA = 1.0 to 3.83 at SSA = 0.85.

As illustrated in the section 4.1, the aerosol radiative effects reduce the precipitation. With the increase of absorption (i.e., decrease of SSA), the accumulated rain per grid averaged over 120 to 480 min decreases significantly (Table 6). The reduction in precipitation with the decrease of SSA is likely caused by the increase in thermal stability from the BC-induced surface cooling and atmospheric heating, which inhibits cloud formation and dries the clouds. The suppressed precipitation has also been found in a study over the east of Asia on the radiative effect of core-coated internally mixed aerosols containing BC [*Huang et al.*, 2007].

5. Conclusion

A spectral-bin cloud-resolving model Goddard Cloud Ensemble (GCE) coupled with a Goddard radiation scheme and an explicit land surface model has been employed to investigate the radiative effects of core-coated internally mixed aerosols containing BC on the deep convective clouds. An aerosol radiative module has been developed to online calculate the wavelength-dependent aerosol radiative properties on the basis of the aerosol composition, size distribution, mixing state, and ambient relative humidity. The sensitivity of cloud properties and the associated radiative forcing to aerosol single-scattering albedo (SSA) have also been examined.

Aerosol radiative effects on cloud properties are pronounced for mid-visible SSA of 0.85. Relative to the case excluding the ARE, cloud fraction and optical depth decrease by about 18% and 20%, respectively. Cloud droplet and ice particle number concentrations, LWP, IWP, and droplet size decrease significantly when the ARE is introduced. The results also reveal that the ice microphysical properties respond much more significantly to the ARE than the warm-rain microphysical properties. The ARE causes a surface cooling of about 0.35 K and significantly high heating rates in the lower troposphere (about 0.6 K day^{-1} higher at 2 km), both of which lead to a more stable atmosphere and hence weaker convection. The semi-direct effect of aerosols dries the atmosphere and burns the cloud layer. The weaker convection and the more desiccation of cloud layers explain the less cloudiness, lower cloud optical depth, less LWP and IWP, smaller droplet size, and less precipitation resulting from the ARE. The daytime-mean

direct forcing induced by black carbon is about 2.2 W m^{-2} at the TOA and -17.4 W m^{-2} at the surface for SSA = 0.85. The positive semi-direct forcing of 11.2 W m^{-2} compensates the negative direct forcing at the surface, causing a much less negative forcing. Both the TOA and surface total radiative forcing values are strongly negative for the deep convective clouds, about -11.6 and -31.9 W m^{-2}, respectively, attributed mostly to aerosol indirect forcing.

Aerosol direct and semi-direct effects are very sensitive to SSA. The TOA semi-direct forcing increases significantly with the decrease of SSA by decreasing the upwelling radiative fluxes due to the increase of aerosol absorption. At the surface, decreasing SSA (increasing absorption) leads to a significant reduction of direct forcing, and a significant increase of semi-direct forcing. Because the positive semi-direct forcing compensates the negative direct forcing at the surface, the surface temperature and heat fluxes decrease less significantly. The aerosol indirect forcing is dominant for deep convective clouds. The cloud fraction, optical depth, convective strength, and precipitation decrease with the increase of absorption, resulting from a more stable and dryer atmosphere due to enhanced surface cooling and atmospheric heating.

Our studies reveal that the aerosol effects on clouds and precipitation are strongly dependent on aerosol properties and cloud thermodynamic and dynamic conditions. In our previous work of a cumulus cloud initiated by a warm bubble, aerosol indirect effects are found to be dominant and lead to stronger convection, larger cloud coverage, and enhanced precipitation [*Fan et al.*, 2007a, b]. However, for absorbing aerosols and the clouds induced by

surface heat fluxes through radiation, aerosol radiative effects are significant, which suppress convection and lead to less cloud fraction, lower cloud optical depth, and less precipitation.

Acknowledgments

This study was partially supported by NSF (ATM-0424885). J. Fan was supported by NASA Headquarters under the Earth System Science (ESS) Fellowship. W.-K. Tao was supported by the NASA Headquarters Atmospheric Dynamics and Thermodynamics Program and the NASA TRMM, and the Office of Science (BER), U.S. DOE (No. DE-AI02-06ER64177). The authors thank Stephen E. Lang and Chung-Lin Shie of NASA/GSFC for help with the radiation transfer model, Jerome Fast of PNNL for observed aerosol optical data, and Robert J. Zamora of NOAA for help with the observed surface data. Tianle Yuan is thanked for the satellite observations of cloud optical depth.

References

Ackerman, A. S., et al. (2000), Reduction of tropical cloudiness by soot, *science*, *288*, 1042-1047.

Ackerman, T. P. and O. B. Toon (1981), Absorption of visible radiation in atmosphere containing mixtures of absorbing and non-absorbing particles, *Appl. Optics*, *20*, 3661-3667.

Alonge, C. J., K. I. Mohr, and W.-K. Tao (2007), Numerical case studies of wet vs. dry regimes in the West African Sahel. *J. Hydrometeor.*, *8*, 102–116.

Baker, R. D., B. H. Lynn, A. Boone, W.-K. Tao, and J. Simpson (2001), The influence of soil moisture, coastline curvature, and land-breeze circulations on sea-breeze initiated precipitation. *J. Hydrometeor.*, *2*, 193-211.

Bohren, C. F., D. R. Huffman (1983), Absorption and scattering of light by small particles, *John Wiley & Sons*, New York.

Brock, C. A., M. Trainer, T. B. Ryerson, J. A. Neuman, D. D. Parrish, J. S. Holloway, D. K. Nicks Jr., G. J. Frost, G. Hubler, F. C. Fehsenfeld, J. C. Wilson, J. M. Reeves, B. G. Lafleur, H. Hilbert, E. L. Atlas, S. G. Donnelly, S. M. Schauffler, V. R. Stroud, and C. Wiedinmyer (2003), Particle growth in urban and industrial plumes in Texas, *J. Geophys. Res.*, *107*(D12), doi:10.1029/2001JD002746.

Businger, J .A., J. C. Wyngaard, Y. Izumi, and E. F. Bradley (1971), Flux-profile relationships in the atmospheric surface layer. *J. Atmos. Sci.*, *28*, 181-189.

Charlson, R. J. and M. J. Pilat (1969), Climate: The influence of aerosols, *J. Appl. Meteorol.*, *8*, 1001–1002.

Chazette, P., and C. Liousse (2001), A case study of optical and chemical ground apportionment for urban aerosols in Thessaloniki, *Atmos. Environ.*, *35*, 2497–2506.

Chylek, P., G. Videen, D. Ngo, R. G. Pinnick, and J. D. Klett (1995), Effect of black carbon on the optical properties and climate forcing of sulfate aerosols, *J. Geophys. Res.*, *100*, 16,325-16,332.

Chou, M.-D., M. J. Suarez (1999), A shortwave radiation parameterization for atmospheric studies, *15*, *NASA/TM-104606*, pp 40.

Chou, M.-D., K.-T. Lee, S.-C. Tsay, Q. Fu (1999), Parameterization for cloud longwave scattering for use in atmospheric models, *J. Clim.*, *12*, 159–169.

Coakley Jr., J. A., R. D. Cess, and F. B. Yurevich (1983), The effect of tropospheric aerosols on the earth's radiation budget: A parameterization for climate models, *J. Atmos. Sci.*, *40*, 116–138.

Fan, J., R. Zhang, G. Li, J. Nielsen-Gammon, and Z. Li (2005), Simulations of fine particulate matter ($PM_{2.5}$) in Houston, Texas, *J. Geophys. Res.*, *110*, D16203, doi:10.1029/2005JD005805.

Fan, J., R. Zhang, D. Collins, and G. Li (2006), Contribution of Secondary Condensable Organics to New Particle Formation: A Case Study in Houston, Texas, *Geophys. Res. Lett.*, *33*, doi:10.1029/2006GL026295.

Fan, J., R. Zhang, G. Li, W.-K. Tao, and X. Li (2007a), Simulations of cumulus clouds using a spectral microphysics cloud-resoving model, *J. Geophys. Res.*, *112*, D04201, doi:10.1029/2006JD007688.

Fan, J., R. Zhang, G. Li, and W.-K. Tao (2007b), Effects of aerosols and relative humidity on cumulus clouds, *J. Geophys. Res.*, in press.

Fast, J. D., W. I. Gustafson Jr., R. C. Easter, R. A. Zaveri, J. C. Barnard, E. G. Chapman, G. A. Grell, and S. E. Peckham (2006), Evolution of ozone, particulates, and aerosol direct radiative forcing in the vicinity of Houston using a fully coupled meteorology-chemistry-aerosol model, *J. Geophys. Res.*, *111*, D21305, doi:10.1029/2005JD006721.

Feingold, G., H. Jiang, and J. Y. Harrington (2005), On smoke suppression of clouds in Amazonia, *Geophys. Res. Lett.*, *32*, L02804, doi:10.1029/2004GL021369.

Hänel, G. (1976), The properties of atmospheric particles as functions of the relative humidity at thermodynamic equilibrium with surrounding moist air, *Adv. Geophys.*, *19*, 73–188.

Hansen, J., M. Sato, and R. Ruedy (1997), Radiative forcing and climate response, *J. Geophys. Res.*, *102*, D6, 6832-6864.

Hegg, A. D., J. Livingston, P. V. Hobbs, T. Novakov, and P. Russell (1997), Chemical apportionment of aerosol column optical depth off the mid-Atlantic coast of the United States, *J. Geophys. Res.*, *102*, 25,293–25,303.

Huang, Y., W. L. Chameides, and R. E. Dickinson (2007), Direct and indirect effects of anthropogenic aerosols on regional precipitation over east Asia, *J. Geophys. Res.*, *112*, D03212, doi:10.1029/2006JD007114.

Intergovernmental Panel on Climate Change (IPCC) (2001), *The Scientific Basis*, Cambridge Univ. Press, New York.

Jacobson, M. Z. (1999), Isolating nitrated and aromatic aerosols and nitrated and aromatic gases as sources of ultraviolet light absorption, *J. Geophys. Res.*, *104*, 3527-3542.

Jacobson, M. Z. (2000), A physically-based treatment of elemental carbon optics: Implications for global direct forcing of aerosols, *Geophys. Res. Lett.*, *27*(2), 217–220.

Jiang, H., and G. Feingold (2006), Effect of aerosol on warm convective clouds: Aerosol-cloud-surface flux feedbacks in a new coupled large eddy model, *J. Geophys. Res.*, *111*, D01202, doi:10.1029/2005JD006138.

Johnson, B. T., K. P. Shine, and P. M. Forster (2004), A semi-direct aerosol effect: Impact of absorbing aerosols on marine stratocumulus, *Q. J. R. Meteorol. Soc.*, *130*, 1407-1422.

Keil, A., and J. M. Haywood (2003), Solar radiative forcing by biomass burning aerosol particles during SAFARI 2000: A case study based on measured aerosol and cloud properties, *J. Geophys. Res.*, *108*(D13), 8467, doi:10.1029/2002JD002315.

Khain, A. P., A. Pokrovsky, M. Pinsky, A. Seifert, and V. Phillips (2004), Simulation of effects of atmospheric aerosols on deep turbulent convective clouds using a spectral microphysics mixed-phase cumulus cloud model. Part I: Model description and possible applications, *J. Atmos. Sci.*, *61*, 2963–2982.

Kratz, D. P., M.-D. Chou, M.-H., Yan, C.-H. Ho (1998), Minor trace gas radiative forcing calculations using the k-distribution method with one-parameter scaling, *J. Geophy. Res.*, *103*, 31647–31656.

Lei, W., R. Zhang, X. Tie, and P. Hess (2004), Chemical characterization of ozone formation in the Houston-Galveston area, *J. Geophys. Res.*, *109*, D12301, doi:10.1029/2003JD004219.

Li, G., R. Zhang, J. Fan, and X. Tie (2005), Impacts of black carbon aerosol on photolysis and ozone, *J. Geophys. Res.*, *110*, D23206, doi:10.1029/2005JD005898.

Li, G., R. Zhang, J. Fan, X. Tie (2007), Impacts of biogenic emissions on photochemical ozone production in Houston, Texas, *J. Geophys. Res.*, in press.

Lynn, B. H., W.-K. Tao, and P.J. Wetzel (1998), A study of landscape generated deep moist convection. *Mon. Wea. Rev.*, *126*, 928-942.

Mallet, M., J. C. Roger, S. Despiau, J. P. Putaud, and O. Dubovik (2004), A study of the mixing state of black carbon in urban zone, *J. Geophys. Res.*, *109*, D04202, doi:10.1029/2003JD003940.

McFarquhar, G. M., and H. Wang (2006), Effects of aerosols on trade wind cumuli over the Indian Ocean: Mosel simulations, *Q. J. R. Meteorol. Soc.*, *132*, 821-843.

Mohr, K. I., R.D. Baker, W.-K. Tao, J.S. Famiglietti, (2003), The sensitivity of West African convection line water budgets to land cover. *J. Hydrometeor.*, *4*, 62-76.

Posfai, M., J. R. Anderson; P. R. Buseck, and H. Sievering (1999), Soot and sulfate aerosol particles in the remote marine troposphere, *J. Geophys. Res.*, *104*, 21,685- 21,693.

Ramachandran, S. (2005), Aerosol radiative forcing over Bay of Bengal and Chennai: Comparison with maritime, continental, and urban aerosol models, *J. Geophys. Res.*, *110*, D21206, doi:10.1029/2005JD005861.

Ramanathan, V., et al. (2001a), The Indian Experiment: An integrated assessment of the climate forcing and the effects of the great indo-asian haze, *J. Geophys. Res.*, *106*, 28,371–28,398.

Ramanathan, V., P. J. Crutzen, J. T. Kiehl, and D. Rosenfeld (2001b), Aerosol, climate and the hydrological cycle, *Science*, *294*, 2119–2124.

Rosenfeld, D. (2000), Suppression of rain and snow by urban and industrial air pollution, *Science*, *287*, 1793–1796.

Tao, W.-K., J. Simpson, D. Baker, S. Braun, M.-D. Chou, B. Ferrier, D. Johnson, A. Khain, S. Lang, B. Lynn, C.-L. Shie, D. Starr, C.-H. Sui, Y. Wang, and P. Wetzel (2003a), Microphysics, radiation, and surface processes in the Goddard Cumulus Ensemble (GCE) model. *Meteor. Atmos. Phys.*, *82*, 97-137.

Tao, W.-K., C.-L. Shie, J. Simpson, S. Braun, R. H. Johnson, and P. E. Ciesielski (2003b), Convective systems over the south China sea: cloud-resolving model simulations, *J. Atmos. Sci.*, *60*, 2929-2956.

Twomey, S. (1977), The influence of pollution on the shortwave albedo of clouds, *J. Atmos. Sci.*, *34*, 1149-1152.

Wang, C. (2004), A modeling study on the climate impacts of black carbon aerosols, *J. Geophys. Res.*, *109*, D03106, doi:10.1029/2003JD004084.

Wetzel, P. J. and A. Boone (1995): A Parameterization for Land-Atmosphere-Cloud Exchange (PLACE), Documentation and testing of a detailed process model of the partly cloudy boundary layer over heterogeneous land. *J. Climate*, *8*, 1810-1837.

Wolf, S. (2002), Mie scattering in particle ensembles under consideration of large size parameter, California Institute of Technology, CA 91125.

Xu, J., M. H. Bergin, R. Greenwald, and P. B. Russell (2003), Direct aerosol radiative forcing in the Yangtze delta region of China: Observation and model estimation, *J. Geophys. Res.*, *108*(D2), 4060, doi:10.1029/2002JD002550.

Zamora, R. J., Wilczak, J. M., Bao, J.-W., and Michelson, S. A. (2003), Heat flux and energy balance in Houston, *A progress report to the Technical Analysis Division, Texas Commission on Environmental Quality (TCEQ)*, May 30.

Zamora, R. J., Dutton, E. G., Trainer M., McKeen, S. A., Wilczak, J. M., and Hou, Y.-T. (2005),

The accuracy of solar irradiance calculations used in mesoscale numerical weather prediction, *Mon. Wea. Rev.*, *133*, 783-792.

Zhang, D., and R. Zhang (2005), Laboratory investigation of heterogeneous interaction of sulfuric acid with soot, *Environ. Sci. Technol., 39*, 5722-5727.

Zhang, R., I. Suh, J. Zhao, D. Zhang, E.C. Fortner, X. Tie, L.T. Molina, and M.J. Molina (2004a), Atmospheric new particle formation enhanced by organic acids, *Science, 304*, 1487-1490.

Zhang, R., W. Lei, X. Tie, P. Hess (2004b), Industrial emissions cause extreme diurnal urban ozone variability, *Proc. Natl. Acad. Sci. USA*, *101*, 6346-6350.

Zhang, R., G. Li, J. Fan, D.L. Wu, E. R. Williams, and M. J. Molina (2007), Intensification of Pacific storm track linked to Asian pollution, *Proc. Natl. Acad. Sci. USA*, *104*, 5295-5299.

Zilitinkevich, S. S. (1975), Comments on "A model for the dynamics of the inversion above a convective boundary layer", *J. Atmos. Sci.*, *32*, 991-992.

Table 1 Selected vegetation and soil characteristics used in PLACE

Vegetation: Broadleaf bushes/trees with groundcover		Soil: sandy clay loam	
Albedo	0.14	Albedo	0.15
% Veg. cover	30%	Porosity	0.42
Leaf area index	4.0	Saturated hydraulic conductivity	6.1×10^{-4}
Root profile layers 1–5	0.00 0.25 0.50 0.20 0.05	Initial soil moisture layers 1–5	0.18–0.21 0.20–0.22 0.23–0.26 0.25–0.28 0.25–0.28
Surface roughness	1.0	% Silt	20%
Minimum stomatal resistance	110.0	% Sand	55%
Biomass heat capacity	5.0	% Clay	25%

Legend: % veg. cover is the percentage of area covered by transpiring vegetation; root profile is the cumulative frequency distribution of roots in the 5 soil moisture reservoirs; surface roughness in m; minimum stomatal resistance is in s m^{-1}; surface biomass (water-equivalent) heat capacity in J K^{-1} m^{-2}. For soil, saturated hydraulic conductivity in m s^{-1}. Initial soil moisture is expressed as volumetric (cm^3 cm^{-3}) soil moisture, the ratio of the volume of soil water to total soil volume.

Table 2 Aerosol properties in numerical simulations

Cases	Composition [a]	Conc. (cm^{-3}) [b]	AOD [c]	SSA [c]	AF [c]
NAR_00	0.9 Ammo. Sulf. 0.1 BC	4.2×10^4	0.0	0.0	0.0
AR_85	0.9 Ammo. Sulf. 0.1 BC	4.2×10^4	0.27	0.85	0.76
SA_100	1.0 Ammo. Sulf.	4.2×10^4	0.25	1.00	0.76
SAC_100	1.0 Ammo. Sulf.	3×10^3	0.009	1.00	0.72

[a] Based on mass mixing ratios.

[b] The concentration is the sum over the aerosol size distribution $dN/d\ln(D_p)$

[c] Values shown here are at the wavelength of 0.55 μm.

Table 3 Cloud properties averaged over 120-480 min for the simulations NAR_00, AR_85, SA_100, and SAC_100

Cases	N_c (cm^{-3})	N_i (cm^{-3})	LWP ($g\ m^{-2}$)	IWP ($g\ m^{-2}$)	r_e (μm)	τ_c	f_{cld}	v_{max} (m/s)	r_{rain} (mm/hr)
NAR_00	191.15	34.38	335.69	1944.99	5.85	4.83	0.18	4.98	0.06
AR_85	203.19	22.85	286.91	1684.01	5.59	3.83	0.15	4.56	0.03
SA_100	253.27	31.07	337.88	1721.31	5.50	5.06	0.18	4.82	0.06
SAC_100	12.98	5.11	314.34	1447.58	12.20	1.34	0.21	4.95	0.11

Table 4 Estimates of radiative forcing for AR_85

$W\ m^{-2}$	TOA	SFC
f_{total}	-11.6	-31.9
$f_{direct+semi}$	12.2	-6.2
f_{direct}	2.2	-17.4
f_{semi}	10.0	11.2
$f_{indirect}$	-23.8	-25.7

Table 5 The solar radiative fluxes for different SSA and the relative forcing to pure ammonium sulfate (SSA=1.0)

SSA	$F^{\downarrow}$(TOA)	$F^{\uparrow}$(TOA)	$F^{\downarrow}$(SFC)	$F^{\uparrow}$(SFC)	F_{net} (TOA)	F_{net} (SFC)	Net fluxes relative to SSA=1.0	
							TOA	SFC
0.85	986.81	-106.62	657.15	-7.57	880.18	649.58	14.05	-5.81
0.90	986.81	-112.81	658.24	-7.40	874.00	650.85	7.86	-4.55
0.95	986.81	-119.15	659.02	-7.31	867.66	651.71	1.53	-3.68
1.00	986.81	-120.67	662.62	-7.23	866.13	655.39	0.00	0.00

Table 6 Cloud and surface fields for different SSA.

SSA	τ_c	f_{cld}	v_{max} (m/s)	Accum. rain per grid (mm)	T_{sfc} (K)	F_{SH} (W m^{-2})	F_{LH} (W m^{-2})
0.85	3.83	0.15	4.56	0.19	305.98	207.67	233.48
0.90	4.15	0.16	4.62	0.28	306.03	210.88	234.57
0.95	4.45	0.17	4.81	0.34	306.06	212.74	235.27
1.00	5.06	0.18	4.82	0.37	306.09	213.88	235.72

Figure captions

Figure 1. Initial profiles of temperature (T), dew point (Td), water vapor mixing ratio (w), and horizontal winds u and v from a sounding near Houston at 7:00 am on August 24, 2000.

Figure 2. Time series of (a) the surface temperature and (b) the downwelling surface infrared fluxes from model simulation AR_85 (solid line) and observations (diamond).

Figure 3. Time series of (a) cloud droplet number concentration, (b) ice particle number concentration, (c) LWP, and (d) IWP averaged over the cloud fields for NAR_00 (solid) and AR_85 (dotted).

Figure 4. (a) Time series of average cloud droplet effective radius (r_e), and (b) the vertical profiles of average r_e for NAR_00 and AR_85.

Figure 5. Time series of average updraft velocity for NAR_00 and AR_85. The values are averaged over the velocities greater than 1.0 m/s.

Figure 6. Time series of average (a) surface temperature, (b) sensible heat flux, and (c) latent heat flux for NAR_00 and AR_85.

Figure 7. Time series of (a) cloud fraction, (b) averaged cloud optical depth over the domain for NAR_00 (solid), AR_85 (dotted), SA_100 (dashed), and SAC_100 (dash-dotted).

Figure 8. Vertical profiles of the heating rates averaged over the horizontal domain for NAR_00, AR_85, SA_100, and SAC_100.

Figure 9. Time series of the accumulation rain per grid for NAR_00, AR_85, SA_100, and SAC_100.

Figure 10. Vertical profiles of the heating rates averaged over the horizontal domain for SSA of 0.85 (solid), 0.90 (dotted), 0.95 (dashed), and 1.00 (dash-dotted).

Figure 11. The aerosol raidative forcing vs. SSA at the (a) TOA and (b) surface.

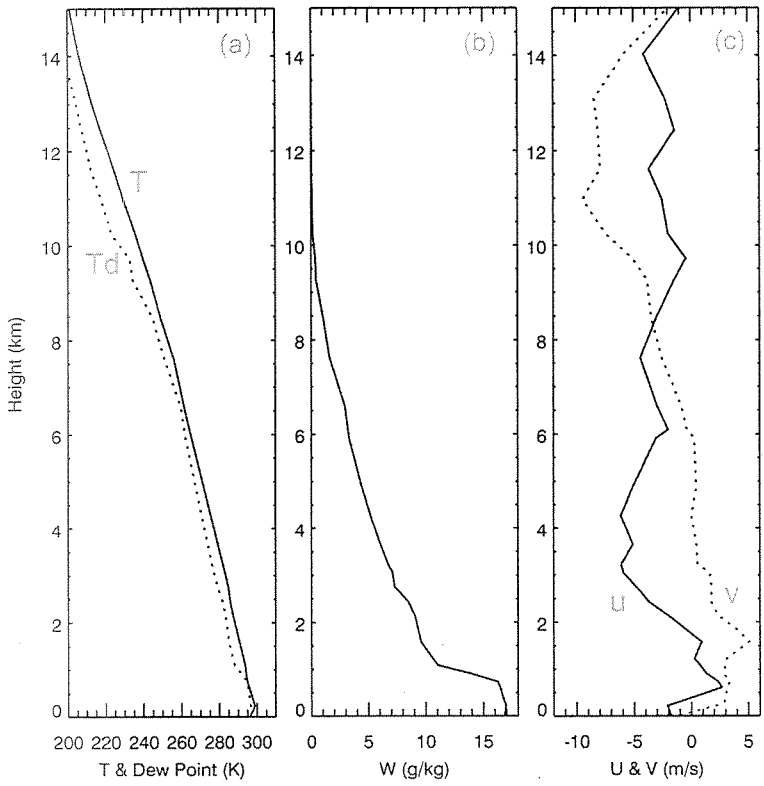

(a)
(b)
(c)
T
Td
u
v
Height (km)
0
2
4
6
8
10
12
14
200 220 240 260 280 300
T & Dew Point (K)
0 5 10 15
W (g/kg)
-10 -5 0 5
U & V (m/s)

Figure 1.

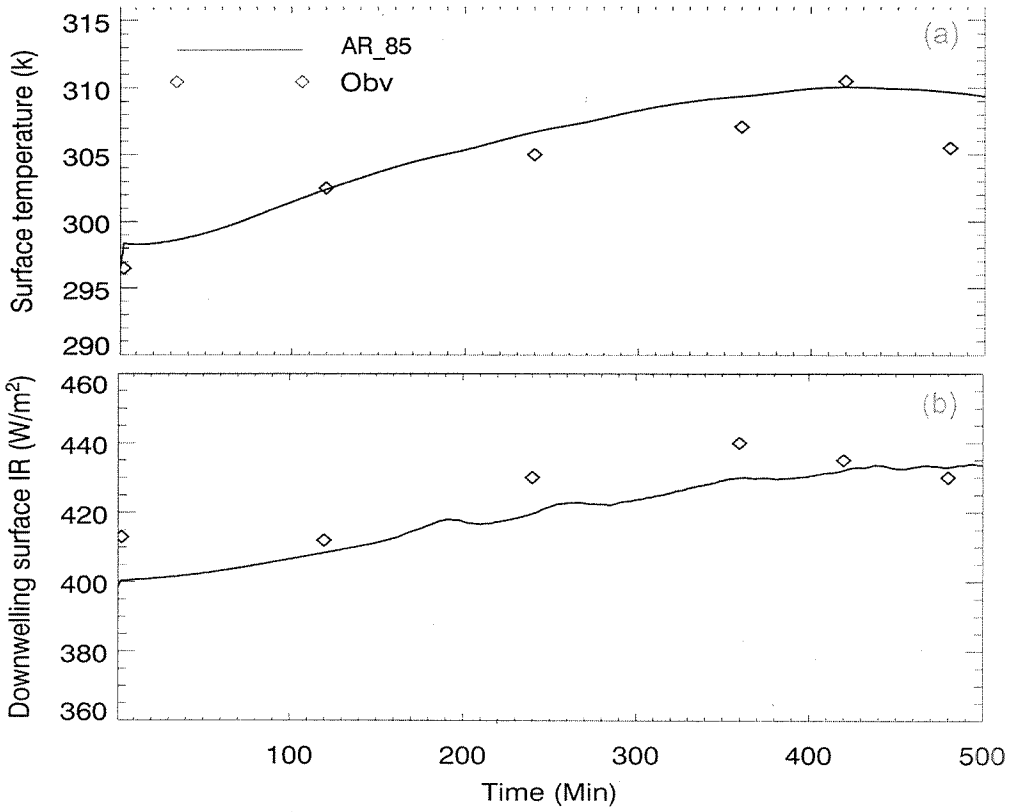

Surface temperature (k)
315
310
305
300
295
290
AR_85
Obv
(a)
Downwelling surface IR (W/m^2)
460
440
420
400
380
360
(b)
100
200
300
400
500
Time (Min)

Figure 2.

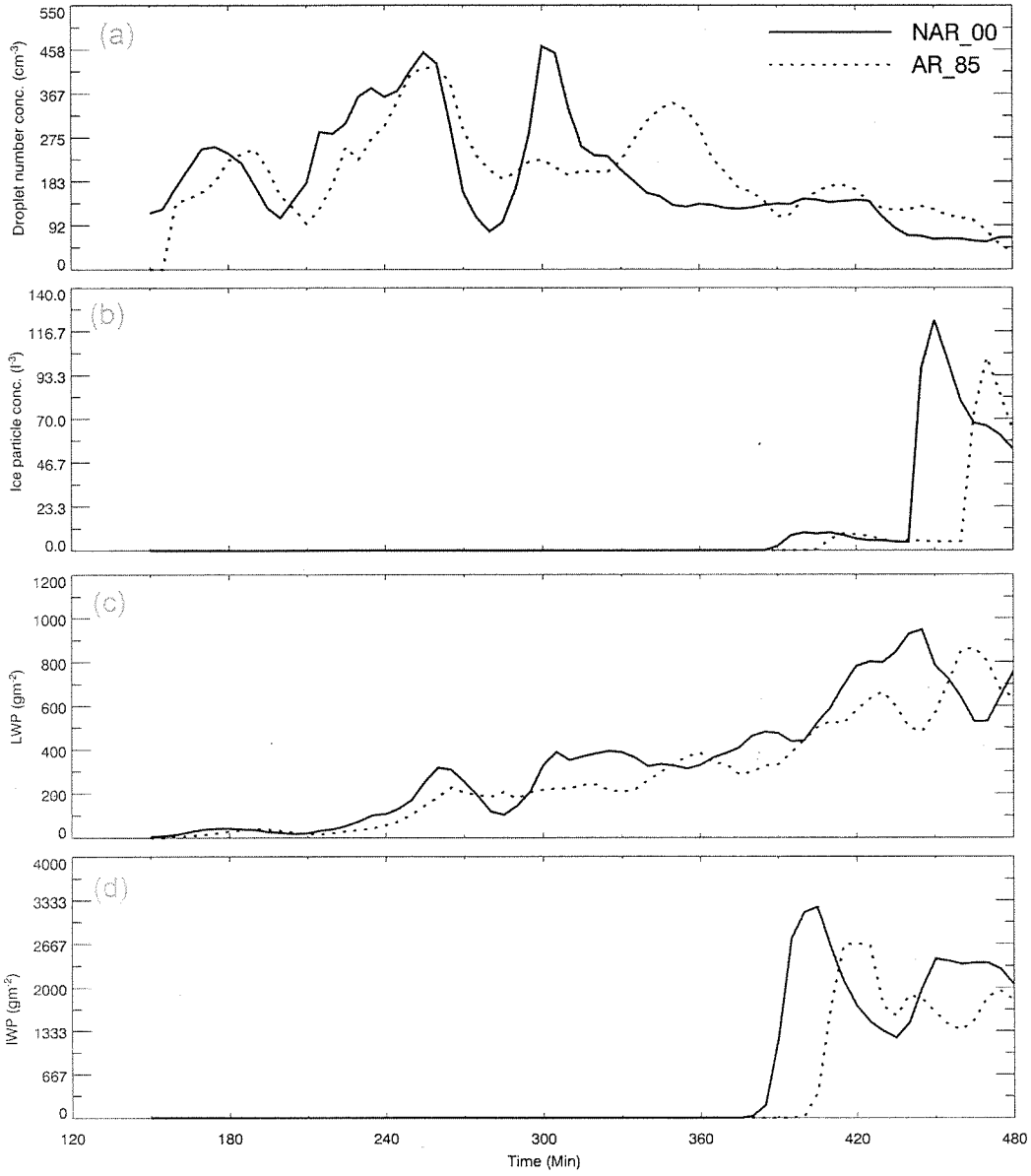

(a)
NAR_00
AR_85
Droplet number conc. (cm-3)
550
458
367
275
183
92
0
(b)
Ice particle conc. (l-1)
140.0
116.7
93.3
70.0
46.7
23.3
0.0
(c)
LWP (gm-2)
1200
1000
800
600
400
200
0
(d)
IWP (gm-2)
4000
3333
2667
2000
1333
667
0
120
180
240
300
360
420
480
Time (Min)

Figure 3.

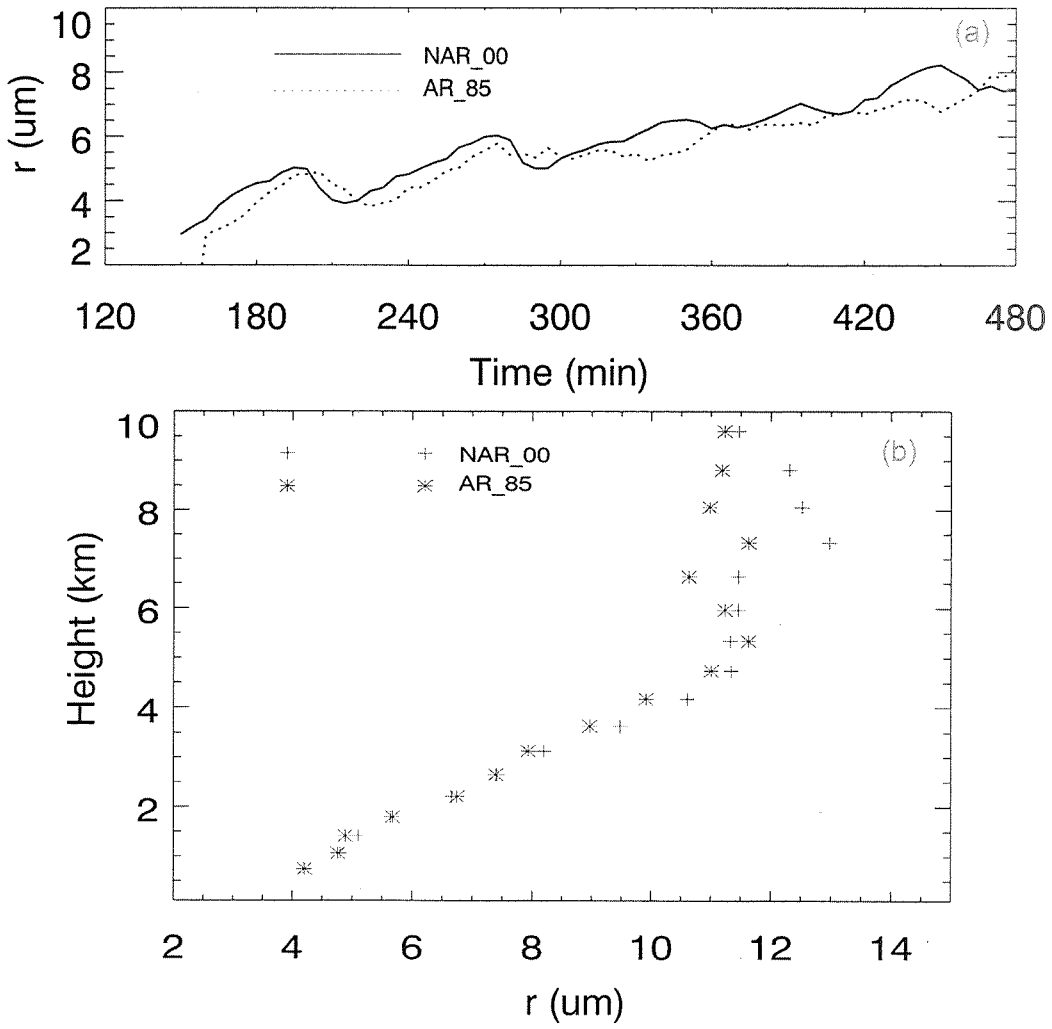


Figure 4.

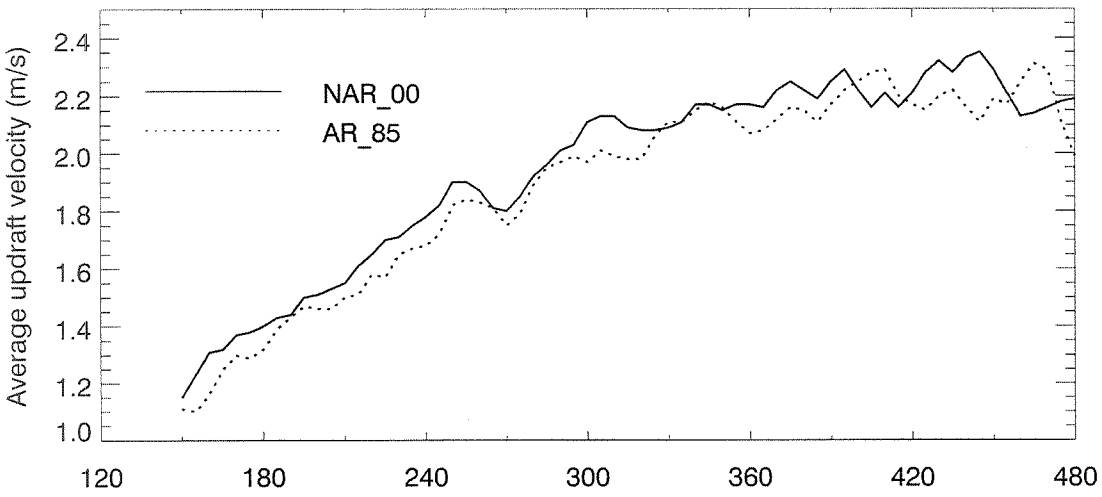

Average updraft velocity (m/s)
2.4
2.2
2.0
1.8
1.6
1.4
1.2
1.0
NAR_00
AR_85
120
180
240
300
360
420
480

Figure 5.

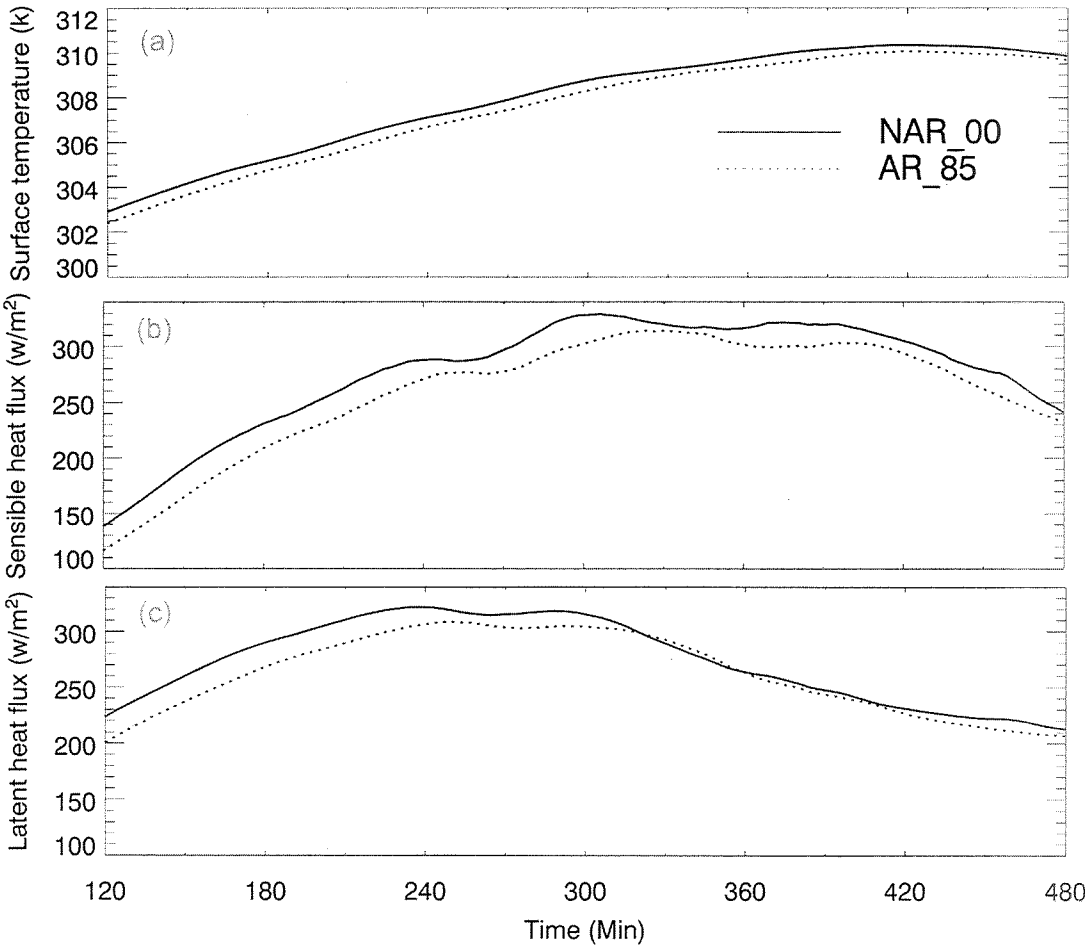

(a)
(b)
(c)
NAR_00
AR_85
Surface temperature (k)
Sensible heat flux (w/m2)
Latent heat flux (w/m2)
312
310
308
306
304
302
300
300
250
200
150
100
300
250
200
150
100
120
180
240
300
360
420
480
Time (Min)

Figure 6.

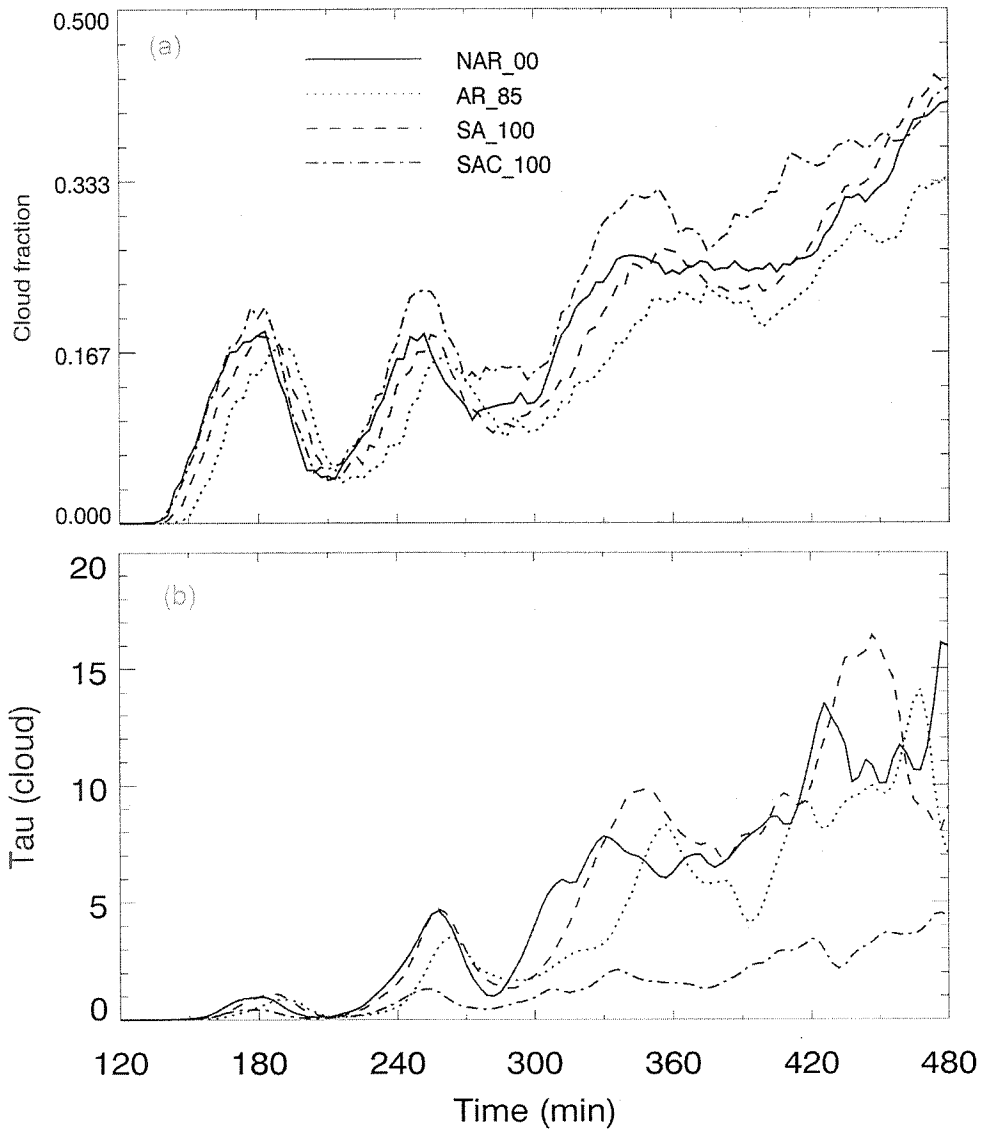

(a)
NAR_00
AR_85
SA_100
SAC_100
Cloud fraction
0.500
0.333
0.167
0.000
(b)
Tau (cloud)
20
15
10
5
0
120
180
240
300
360
420
480
Time (min)

Figure 7.

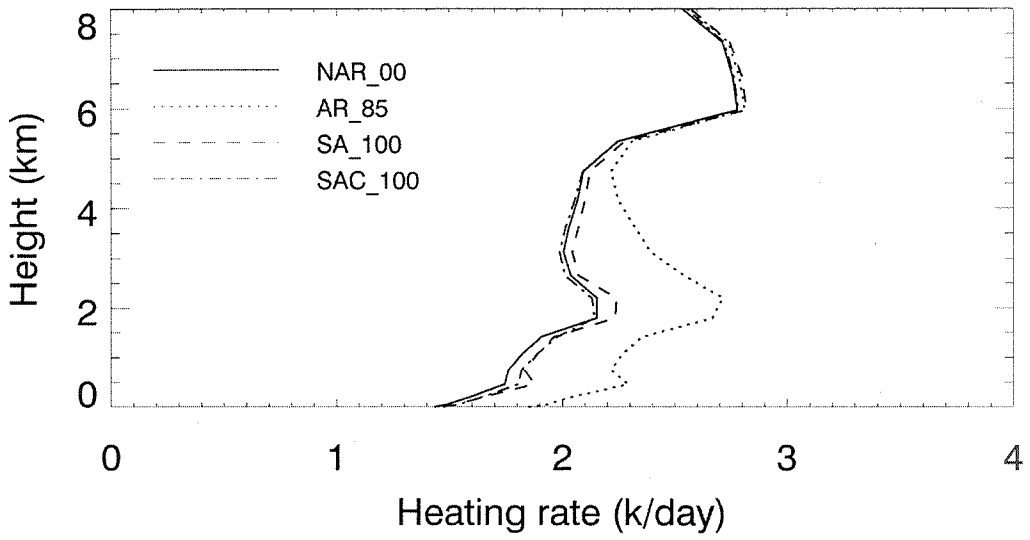


Figure 8.

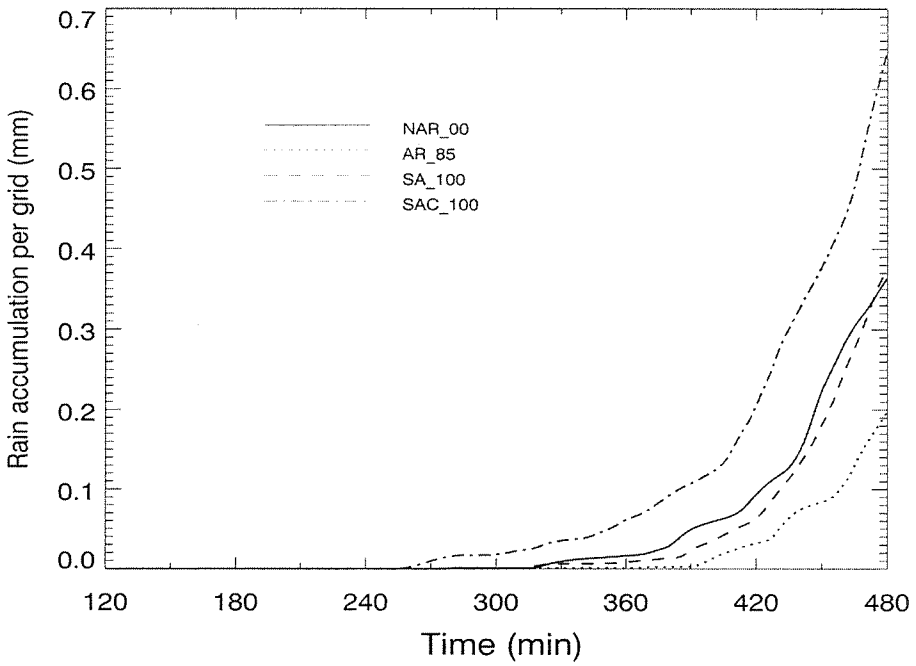


Figure 9.

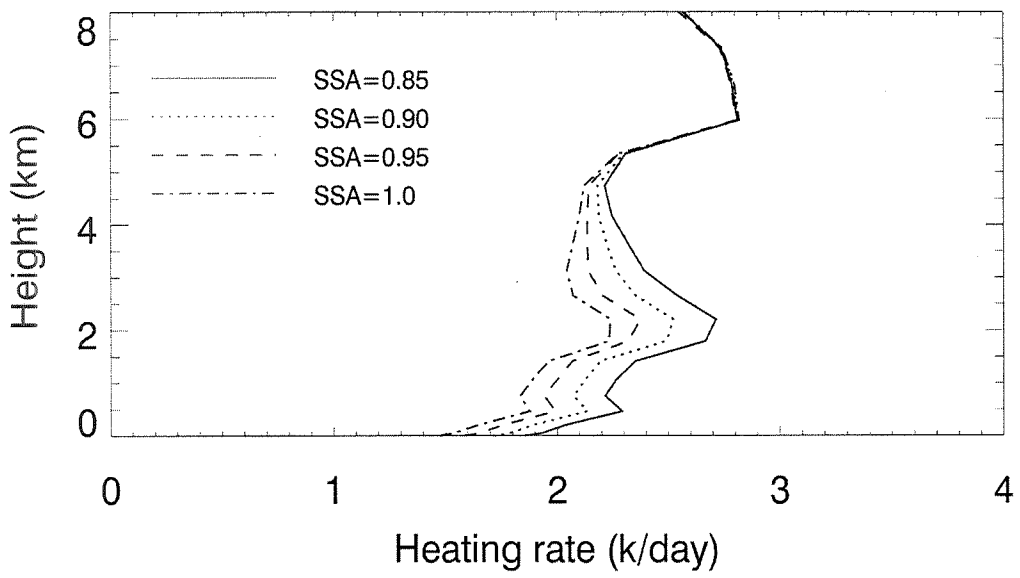


Figure 10.

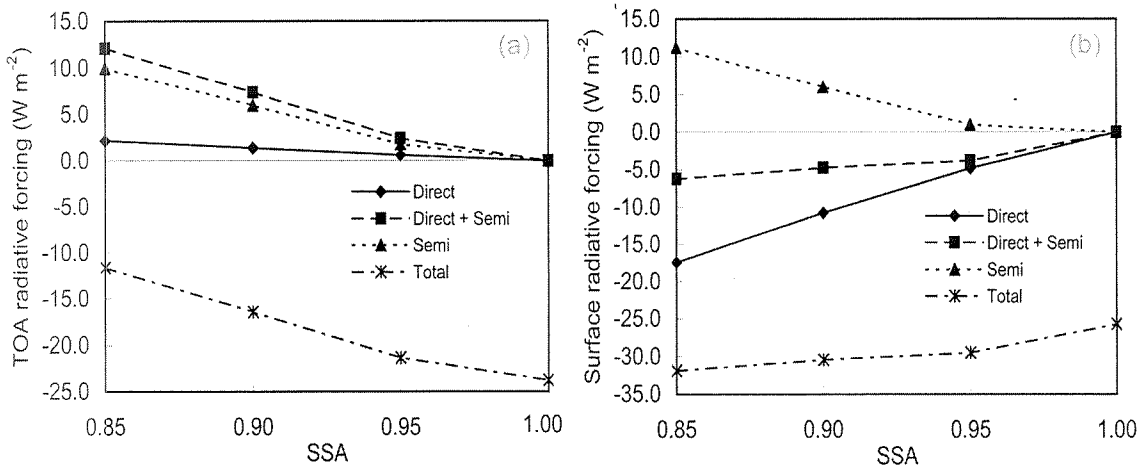


Figure 11.